

Quantum cascade laser investigations of CH₄ and C₂H₂ interconversion in hydrocarbon/H₂ gas mixtures during microwave plasma enhanced chemical vapor deposition of diamond

Jie Ma,¹ Andrew Cheesman,¹ Michael N. R. Ashfold,^{1,a)} Kenneth G. Hay,² Stephen Wright,² Nigel Langford,² Geoffrey Duxbury,² and Yuri A. Mankelevich³

¹*School of Chemistry, University of Bristol, Bristol BS8 1TS, United Kingdom*

²*Department of Physics, University of Strathclyde, John Anderson Building, 107 Rottenrow, Glasgow G4 0NG, United Kingdom*

³*Skobel'tsyn Institute of Nuclear Physics, Moscow State University, Leninskie Gory, Moscow 119991, Russia*

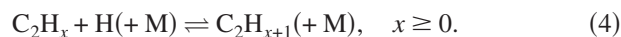
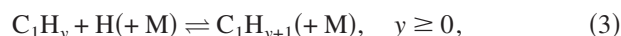
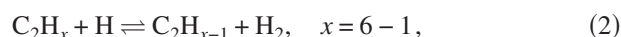
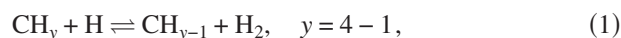
(Received 31 July 2008; accepted 19 June 2009; published online 5 August 2009)

CH₄ and C₂H₂ molecules (and their interconversion) in hydrocarbon/rare gas/H₂ gas mixtures in a microwave reactor used for plasma enhanced diamond chemical vapor deposition (CVD) have been investigated by line-of-sight infrared absorption spectroscopy in the wavenumber range of 1276.5–1273.1 cm⁻¹ using a quantum cascade laser spectrometer. Parameters explored include process conditions [pressure, input power, source hydrocarbon, rare gas (Ar or Ne), input gas mixing ratio], height (*z*) above the substrate, and time (*t*) after addition of hydrocarbon to a pre-existing Ar/H₂ plasma. The line integrated absorptions so obtained have been converted to species number densities by reference to the companion two-dimensional (*r, z*) modeling of the CVD reactor described in Mankelevich *et al.* [J. Appl. Phys. **104**, 113304 (2008)]. The gas temperature distribution within the reactor ensures that the measured absorptions are dominated by CH₄ and C₂H₂ molecules in the cool periphery of the reactor. Nonetheless, the measurements prove to be of enormous value in testing, tensioning, and confirming the model predictions. Under standard process conditions, the study confirms that all hydrocarbon source gases investigated (methane, acetylene, ethane, propyne, propane, and butane) are converted into a mixture dominated by CH₄ and C₂H₂. The interconversion between these two species is highly dependent on the local gas temperature and the H atom number density, and thus on position within the reactor. CH₄ → C₂H₂ conversion occurs most efficiently in an annular shell around the central plasma (characterized by 1400 < *T*_{gas} < 2200 K), while the reverse transformation C₂H₂ → CH₄ is favored in the more distant regions where *T*_{gas} < 1400 K. Analysis of the multistep interconversion mechanism reveals substantial net consumption of H atoms accompanying the CH₄ → C₂H₂ conversion, whereas the reverse C₂H₂ → CH₄ process only requires H atoms to drive the reactions; H atoms are not consumed by the overall conversion. © 2009 American Institute of Physics. [DOI: 10.1063/1.3176971]

I. INTRODUCTION

Microwave (MW) plasma activation of dilute hydrocarbon in hydrogen gas mixtures finds widespread use as a route to growing high quality diamond films by chemical vapor deposition (CVD) methods.^{1–4} As discussed previously,⁵ the H₂ molecules dissociate following excitation within the plasma ball, and the resulting H atoms diffuse throughout the reactor volume. The lack of efficient H atom loss processes in these gas mixtures ensures that H atom densities in the cooler periphery of the reactor are far in excess of those expected on the basis of local thermodynamic equilibrium. H atoms fulfill a number of important roles in the CVD process—both in the gas phase and at the gas-surface interface. The studies described here focus on aspects of the former, where H atoms drive radical formation via the so-called “H-shifting” abstraction reactions (1) and (2) and, in

the cooler regions, third-body stabilized H addition reactions (3) and (4) that culminate in the interconversion between C₁(CH_{*y*}) and C₂(C₂H_{*x*}) species,^{1,6}



Interconversions between CH_{*y*} and C₂H_{*x*} species occur on timescales that are much shorter than the transit time for feedstock gas through most CVD reactors, leading to the expectation that the distribution of CH_{*y*}, C₂H_{*x*}, etc., species present in an activated hydrocarbon/H₂ gas mixture should be rather insensitive to the choice of hydrocarbon feedstock gas. Such a view is supported by early studies⁷ demonstrating growth of diamond films with similar morphologies and at similar rates from a range of different hydrocarbon source

^{a)} Author to whom correspondence should be addressed. Tel.: (117)-9288312/3. FAX: (117)-9250612. Electronic mail: mike.ashfold@bris.ac.uk.

gases (at a constant input carbon mole fraction), and by Fourier transform infrared absorption⁸ and molecular beam mass spectrometry^{9,10} measurements of the densities of various of the more abundant stable species (e.g., CH₄, C₂H₂, and C₂H₄) in MW activated CH₄/H₂ and C₂H₂/H₂ gas mixtures. Both of these gas phase diagnostic experiments had some limitations, however. The former gave no spatial information, while the latter only returned relative (rather than absolute) concentrations.

There is a continuing need for new and improved, quantitative, nonintrusive, *in situ* probes of the gas phase chemistry and composition, both to refine our understanding of the diamond CVD process and for improved process control applications. Celii *et al.*^{11,12} demonstrated the potential applicability of infrared tunable diode laser absorption spectroscopy methods for detecting CH₃ radicals, and C₂H₂ and C₂H₄ molecules, in HF activated CH₄/H₂ gas mixtures in the late 1980s, but the subsequent take-up of such methods has been slow. In part, this is because such methods provide line-of-sight absorbances, which can only be turned into absolute column (or number) densities given detailed knowledge of the (generally very inhomogeneous) distribution of species concentrations and temperatures along the viewing column. Measurements of this kind are thus of limited quantitative value in the absence of companion high level reactor modeling. Such detailed studies are now starting to appear, however—notably measurements of CH₃ radicals, as well as the stable species C₂H₂, CH₄, and C₂H₆, in MW activated CH₄/H₂ mixtures in a quartz bell jar reactor used for diamond CVD.^{13–15}

We recently demonstrated¹⁶ the use of a quantum cascade (QC) laser^{17–19} for probing CH₄ and C₂H₂ molecules, and their interconversion, in a 2 kW MW reactor operating with both CH₄/Ar/H₂ and C₂H₂/Ar/H₂ feedstock gas mixtures, as a function of process conditions (e.g., input hydrocarbon mole fraction, total gas pressure, and applied MW power). We also exploited the rapid output frequency sweep (“chirp”) rate of pulsed QC lasers to gain insights into the time evolution of the CH₄/C₂H₂ ratio when either is introduced into, or removed from, a pre-existing Ar/H₂ plasma. Here we present higher sensitivity single pass QC laser absorption measurements of CH₄ and C₂H₂ molecules, and their interconversion, in this MW reactor, as functions of the above process conditions, the H₂/Ar mixing ratio, and vertical distance (z) above the substrate surface for a wider variety of feedstock hydrocarbon source gases (not only methane and acetylene but also *n*-propane, *n*-butane, ethene, and propyne). These data serve to demonstrate the efficiency with which all precursor hydrocarbons are processed to (locally equilibrated) mixtures dominated by CH₄ and C₂H₂ under typical CVD conditions. As noted previously,^{14–16} gas temperature and number density considerations dictate that the bulk of the monitored CH₄ and C₂H₂ molecules are localized in the cooler periphery of the reactor, remote from the plasma ball. Complementary, spatially resolved, column density measurements of radical species [C₂(a) and CH(X)] and of electronically excited H($n=2$) atoms—obtained by cavity ring down spectroscopy—are described elsewhere.²⁰ These transient species are concentrated in the plasma ball itself.

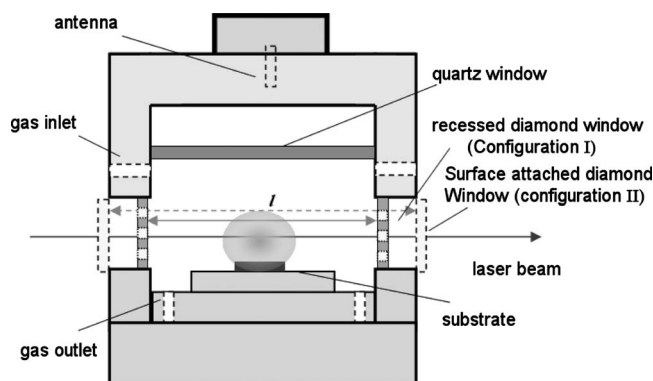


FIG. 1. Schematic diagram of the CVD reactor illustrating the position of the substrate, plasma ball, and the windows for optical probing using configurations I and II.

Both data sets serve to tension and validate the detailed two-dimensional (2D) modeling of the gas phase chemistry prevailing in this high pressure MW CVD reactor.⁵

II. EXPERIMENTAL

Details of the custom-designed MW reactor (2 kW, 2.45 GHz Muegge power supply and generator) and of the QC laser spectrometer (Cascade Technologies Ltd., operating with a 7.85 μm laser) have been presented previously.¹⁶ Here we detail improvements implemented since the initial study. One enhancement involved changes to the reactor viewing apertures. The 4 mm diameter apertures that defined the previous viewing column have been replaced by two 25 mm(vert.) \times 5.5 mm(horiz.) slot apertures, which allow operation of the reactor in two configurations as illustrated in Fig. 1. In configuration I, each slot is sealed by thin rectangular polished CVD diamond windows (Element Six Ltd.) mounted on wedged flanges to reduce etalon effects, thereby maintaining the same ($l=19$ cm) column length as before. Alternative, matched flanges are used in configuration II. Each of these flanges is fabricated with a tongue that projects into the slot aperture and supports three 5.8 mm diameter, wedged (2°), thin (300 μm) diamond windows (the centers of which are, respectively, 1, 11, and 21 mm above the substrate surface). Countersinking the windows reduces the column length to $l=14$ cm, thereby reducing the (dominant) contribution to absorption from cold gas at the ends of the viewing column. The second improvement allows for spatial profiling. The complete optical assembly (laser, beam steering optics, and detector) is now mounted on a rigid platform that can be translated vertically, with better than 1 mm precision, relative to the fixed MW reactor—thereby enabling spatially resolved, line-of-sight column density measurements with configuration I as a function of z , the vertical distance above the top surface of the 30 mm diameter Mo substrate. z values were read from a rigidly mounted vernier scale, and $z=0$ determined by finding the platform setting at which the substrate first impeded transmission of the probe laser beam. The third improvement involves the detectivity of the QC laser spectrometer. The liquid nitrogen cooled mercury cadmium telluride (MCT) detector with external transimpedance amplifier used previously to monitor the

TABLE I. Wavenumbers, assignments, and $S(T)$ line strength factors (Ref. 21) of CH_4 transitions observed in the wavenumber range of 1276.5–1273.1 cm^{-1} .

Wavenumber (cm^{-1})	Line intensity [$10^{-24} \text{ cm}^{-1}(\text{mol cm}^{-2})^{-1}$]				E'' (cm^{-1})	Vibrational transition	Rotational transition	C isotope
	298	K	450 K	3000 K				
1276.331 05	123		639	8.21	1433.9722	4_1^2	$3F_{25}-4F_{13}$	12
1276.262 06	23.5		55.7	0.192	949.888	4_0^1	$13F_{14}-13F_{21}$	13
1275.945 66	564		2180	17	1250.836	4_0^1	$15F_{24}-15F_{11}$	12
1275.947 76	564		2180	17	1250.837	4_0^1	$15F_{15}-15F_{21}$	12
(Sum)	(1128)		(4360)	(34)				
1275.779 28	671		400	0.139	104.778	4_0^1	$3A_{21}-4A_{11}$	13
1275.621 60	1.51		11.0	0.248	1639.651	$2_1^1 4_0^1$	$4F_{29}-4F_{15}$	12
1275.386 78	24 400		15 900	6.35	157.137	4_0^1	$4E_2-5E_1$	12
1275.326 54	401		240	0.083	104.780	4_0^1	$3F_{22}-4F_{11}$	13
1275.041 68	36 700		23 900	9.53	157.139	4_0^1	$4F_{23}-5F_{12}$	12
1274.984 82	269		159	0.0552	104.781	4_0^1	$3E_2-4E_1$	13
1274.786 13	86.6		62.3	0.0295	219.937	4_0^1	$6F_{11}-6F_{22}$	12
1274.213 93	79.3		413	5.28	1432.524	4_0^1	$3E_3-4E_2$	12
1274.016 90	398		238	0.0823	104.785	4_0^1	$3F_{13}-4F_{21}$	13
1273.881 63	34.7		174	2.09	1409.376	4_1^2	$3E_2-4E_1$	12
1273.875 25	1.66		60.4	19.7	2623.659	4_0^1	$22A_{23}-22A_{11}$	12
1273.864 56	1.00		36.3	11.8	2623.677	4_0^1	$22F_{28}-22F_{12}$	12
1273.858 75	0.669		24.3	7.90	2623.687	4_0^1	$22E_5-22E_2$	12
(Sum)	(3.329)		(121)	(39.4)				
1273.840 15	11.1		119	5.12	1878.424	4_1^2	$10A_{13}-10A_{22}$	12
1273.782 40	13.6		171	9.56	1975.015	4_0^1	$19E_4-19E_1$	12
1273.782 49	20.4		257	14.4	1975.013	4_0^1	$19F_{17}-19F_{22}$	12
1273.782 57	34.0		428	23.9	1975.008	4_0^1	$19A_{13}-19A_{21}$	12
(Sum)	(68.0)		(856)	(47.86)				
1273.469 77	52.2		261	3.13	1409.007	4_1^2	$3F_{14}-4F_{22}$	12
1273.418 31	120		626	7.99	1432.181	4_1^2	$3F_{15}-4F_{23}$	12

transmitted IR intensity was replaced by a new photovoltaic MCT detector with a two stage Peltier cooler and a built-in amplifier (Vigo). This has a built-in immersion lens (enabling improved radiation collection) and a wider bandwidth (that removes most of the overshoot of the pulsed laser signal). As illustrated below, this detector returns spectra with substantially better signal to noise ratios, allowing observation of many weak spectral features not recognized in the original study.

The source gases used, along with suppliers and stated purities, were as follows: CH_4 (BOC, 99.5%), C_2H_2 (BOC, 98.5%), ethene (Argo, 99.7%), *n*-propane (Argo, 99%), *n*-butane (Argo, 99.4%), propyne (Argo, 96%), H_2 (BOC, 99.995%), and Ar and Ne (BOC, 99.995%). The hydrocarbon, H_2 , and Ar(Ne) gas flows were metered through three separate mass flow controllers (MFCs) (mks), calibrated for CH_4 , H_2 , and Ar; flow rates of the neon and the various nonmethane hydrocarbons were derived using the manufacturer correction factors (where available) and, in the case of C_2H_2 , verified independently by IR absorption spectroscopy (see Tables I and II).

III. RESULTS AND DISCUSSION

A. Preamble

To aid the subsequent discussion, absorption spectra of room temperature samples of CH_4 and C_2H_2 recorded over

the wavenumber range of 1276.5–1273.1 cm^{-1} using reactor configuration I are shown in Figs. 2 and 3. The pressures in each case have been chosen deliberately so that the strongest features are saturated, thereby allowing weaker features to be seen more clearly. Lines evident in Fig. 2 are attributable to rovibrational transitions of the 4_0^1 fundamental bands of $^{12}\text{CH}_4$ and $^{13}\text{CH}_4$ (and associated hot bands originating from both the 2_1 and 4_1 levels of $^{12}\text{CH}_4$),²¹ as detailed by the assignment combs in the figure and the listing in Table I. The most intense features in the case of C_2H_2 (Fig. 3) are P branch transitions within the $4_0^1 5_0^1$ combination band of the $^{12}\text{C}_2\text{H}_2$ isotopomer.²¹ Hot band absorptions are again identifiable, originating from levels carrying one and two quanta of excitation in ν_4 and/or ν_5 (the *trans*- and *cis*-bending modes, respectively)²²—as detailed in Table II. Several weak features remain unassigned in Fig. 3; these are most likely attributable to $\text{H}^{12}\text{C}^{13}\text{CH}$.

Measurements of room temperature gas mixtures provide a means of testing the absolute calibration of the MFCs. Plot (b) in Fig. 2 shows the CH_4 number densities obtained by plotting the integrated absorbances (in cm^{-1}) of the $4F_{23}-5F_{12}$ line measured for various *a*% CH_4 /7%Ar/balance H_2 mixtures, scaled by the appropriate $S(298 \text{ K})$ value [$3.67 \times 10^{-20} \text{ cm}^{-1}/(\text{molecule cm}^{-2})$] (Ref. 21)] and then divided by $\ell = 19 \text{ cm}$, against those calculated from the set flow rates and pressure (assuming ideal gas behavior). The gradient of this straight-line correlation is

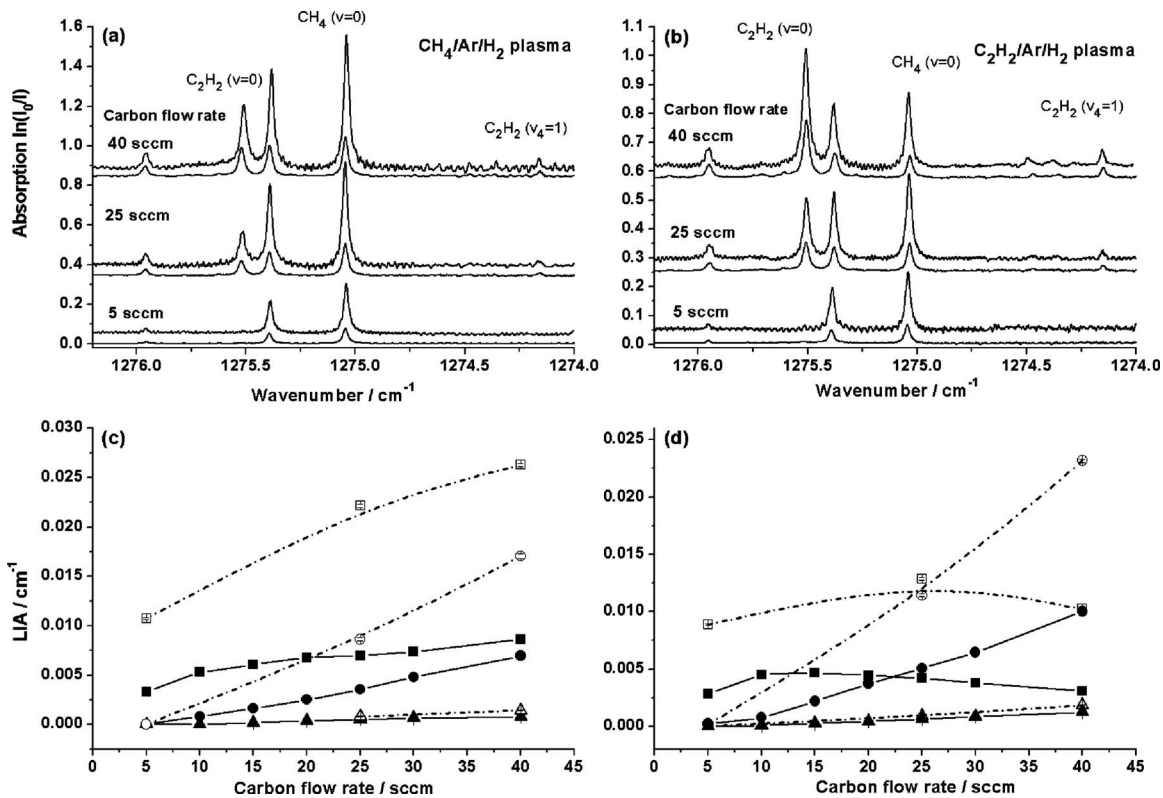


FIG. 4. Absorption spectra of activated (a) $x\%\text{CH}_4/7\%\text{Ar}/\text{H}_2$ and (b) $y\%\text{C}_2\text{H}_2/7\%\text{Ar}/\text{H}_2$ gas mixtures using three different carbon flow rates, recorded over the wavenumber range of $1276.5\text{--}1274.0\text{ cm}^{-1}$. Key CH_4 and C_2H_2 features are labeled; detailed assignments of these transitions are given in Tables I and II. The upper/lower spectrum in each pair was recorded using configuration I/II. For display purposes, the upper of the two spectra measured at each carbon flow rate has been raised vertically by 0.05 absorbance units, and each pair of spectra in each panel has been offset vertically by larger amounts. The total flow rate ($F=565\text{ SCCM}$), pressure ($p=150\text{ Torr}$), and applied MW power ($P=1.5\text{ kW}$) were the same for each of the spectra. (c) and (d) show the LIAs for the $\text{CH}_4\ 4_0^2\ 4F_{23}\text{--}5F_{12}$ (\blacksquare), $\text{C}_2\text{H}_2\ 4_0^2\ 5_0^2\ P(23,e)$ (\bullet), and $\text{C}_2\text{H}_2\ 4_7^2\ 5_0^2\ P(24,f)$ (\blacktriangle) lines of interest, and their variation with carbon flow rate.

the probed column span the range from room temperature to $\sim 3000\text{ K}$.^{5,20} As Table I shows, our relative sensitivity to $\text{CH}_4(v=0, J=19)$ molecules rises >10 -fold and subsequently declines over this temperature range, while our sensitivity to $\text{CH}_4(v=0, J=4)$ molecules drops by $\sim 5 \times 10^3$. Even modest temperature changes can cause significant changes in S factor, as exemplified by the case of the $4_1^2\ P(4)$ transition on increasing T from 300 to 450 K. The T dependence in the case of C_2H_2 is less dramatic, since all of the levels monitored involve broadly similar J values ($J \sim 20$). However, as Table II illustrates, the probed wavelength range allows access to C_2H_2 molecules with $v=0$ ($E'' \sim 650\text{ cm}^{-1}$), $v_{4/5}=1$ ($E'' \sim 1150\text{--}1300\text{ cm}^{-1}$), and $v_{4/5}=2$ ($E'' \sim 1700\text{--}2000\text{ cm}^{-1}$). The temperature dependence of the vibrational partition function will ensure greatest relative sensitivity to the most vibrationally excited C_2H_2 molecules at higher T . The HITRAN database²¹ currently lists $S(T)$ factors for $\text{C}_2\text{H}_2(v=0)$ molecules only, but $S(T)$ factors for other transitions of interest (with $v > 0$) can be estimated as shown in the Appendix.

B. Spatially resolved CH_4 and C_2H_2 absorption and number density profiles

Figure 4 compares and contrasts absorption spectra recorded in the narrower wavenumber range of $1276.2\text{--}1274.0\text{ cm}^{-1}$ with both reactor configurations, at $z=11\text{ mm}$, using $x\%\text{CH}_4/7\%\text{Ar}/\text{balance H}_2$ [Fig. 4(a)] and

$y\%\text{C}_2\text{H}_2/7\%\text{Ar}/\text{balance H}_2$ [Fig. 4(b)] gas mixtures at a total flow rate of $F=565\text{ SCCM}$ (SCCM denotes standard cubic centimeter per minute at STP), pressure $p=150\text{ Torr}$, and applied MW power $P=1.5\text{ kW}$, as functions of the carbon flow rate. For ease of display, the two spectra for each carbon flow recorded with the different experimental configurations have been offset vertically by 0.05 absorbance units, and the pairs of spectra recorded with different carbon flow rates have each been offset vertically by larger amounts. The configuration I measurements are comparable to those reported previously¹⁶ and have thus been repeated at fewer carbon flow rates. The line at 1275.042 cm^{-1} is due solely to $\text{CH}_4(v=0)$ molecules, whereas both $\text{CH}_4(v=0)$ and $\text{C}_2\text{H}_2(v_4=1)$ molecules can contribute to the blended line at $\sim 1275.38\text{ cm}^{-1}$. The peaks at 1275.512 and 1274.156 cm^{-1} are both entirely due to C_2H_2 molecules—in their $v=0$ and $v_4=1$ levels, respectively. The more detailed analysis of the respective parent room temperature absorption spectra reported in Tables I and II shows the remaining line, at $\sim 1275.95\text{ cm}^{-1}$, to be a blended feature, involving contributions from both $\text{C}_2\text{H}_2(v_5=1)$ and $\text{CH}_4(v=0, J=15)$ molecules—rather than being wholly associated with $\text{C}_2\text{H}_2(v_5=1)$ molecules as presumed previously.¹⁶ Figures 4(c) and 4(d) show the line integrated absorbances (LIAs) derived for the various unblended peaks, for both reactor configurations, plotted as functions of “carbon” flow rate

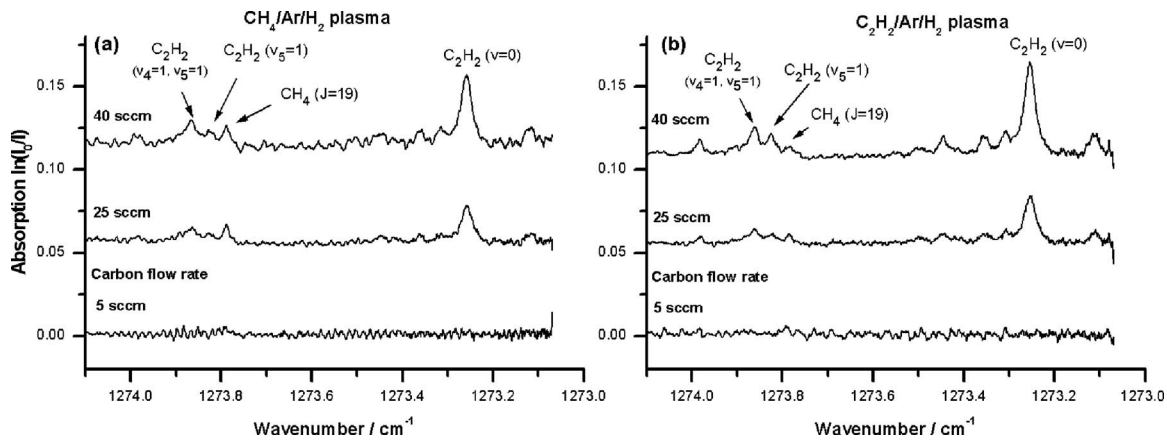


FIG. 5. Absorption spectra of activated (a) $x\%CH_4/7\%Ar/H_2$ and (b) $y\%C_2H_2/7\%Ar/H_2$ gas mixtures using three different carbon flow rates, recorded over the wavenumber range $1274.1-1273.0\text{ cm}^{-1}$ using configuration II at $z=21\text{ mm}$. Selected CH_4 and C_2H_2 features are indicated; detailed assignments of these transitions are given in Tables I and II. For display purposes, the various spectra have been offset vertically. The total flow rate ($F=565\text{ SCCM}$), pressure ($p=150\text{ Torr}$), and applied MW power ($P=1.5\text{ kW}$) were the same for each of the spectra.

(where CH_4 and C_2H_2 flow rates of x and $y\text{ SCCM}$ equate to carbon flow rates of, respectively, x and $2y\text{ SCCM}$).

Several points emerge from these data. The same peaks are apparent in all spectra recorded at a given carbon flow rate, irrespective of the identity of the input hydrocarbon, again emphasizing the efficient methane \leftrightarrow acetylene interconversion. The absorption measured at low (5 SCCM) carbon flow rate is largely attributable to CH_4 , but C_2H_2 absorption features become increasingly evident at higher carbon flow rates. The previous suggestion¹⁶ of a population inversion between the $v_5=1$ and $v=0$ levels of C_2H_2 at low carbon flow rates is incorrect. The $\sim 1275.95\text{ cm}^{-1}$ feature measured at low carbon input fractions is actually attributable to rotationally “hot” CH_4 molecules. None of the data reported here contradicts the assumption that the rotational and vibrational state populations of these stable hydrocarbon species are in local thermodynamic equilibrium. The nonobservation of the (cold) $^{13}CH_4$ feature at 1275.7793 cm^{-1} in spectra recorded at low carbon flow rate serves to reinforce the very different $S(T)$ dependences of this line and of neighboring (hot) CH_4 feature at $\sim 1275.95\text{ cm}^{-1}$ —detailed in Table I. Source gas dependent differences also become more evident in the spectra recorded at higher carbon flow rates. The spectrum recorded with 40 SCCM CH_4 is dominated by the CH_4 feature, whereas the largest peak in the spectrum recorded with 20 SCCM C_2H_2 is due to C_2H_2 . These trends can be seen more clearly in the LIA plots [Figs. 4(c) and 4(d)] and will be discussed in more detail in Sec. III D.

Figures 4(c) and 4(d) also highlight the differences in LIAs measured using configurations I and II. Reducing the length of the viewing column from $l=19$ to $l=14\text{ cm}$ results in varying reductions in all LIAs [by $\sim 66\%$ in the case of CH_4 and by, respectively, $\sim 50\%$ and $\sim 33\%$ in the case of $C_2H_2(v=0)$ and $C_2H_2(v_4=1)$ molecules], reflecting their differing spatial distributions but also reinforcing the model predictions⁵ that most of the CH_4 and C_2H_2 number density is concentrated in the cooler regions near the wall of the reactor. Spectra taken at the lowest (5 SCCM) carbon flow rates show no discernible $C_2H_2(v=0)$ absorption. Thus it is valid to attribute all of the absorption at 1275.95 cm^{-1} in

such spectra to the $CH_4\ 4_0^1 Q15F_{21}$ and F_{11} transitions. Their combined intensity, relative to that of the $CH_4\ 4_0^1 P5F_{12}$ line at 1275.04 cm^{-1} , provides a route for estimating the gas temperature (T_{gas}) in the columns bounded by the water cooled reactor wall that distinguish configurations I and II. Specifically, we calculate the difference in the LIAs (ΔLIA) measured for each line under identical process conditions and compare this ratio with the (temperature dependent) ratio of the respective $S(T)$ line strength factors. The latter ratio varies rapidly with T and matches ΔLIA when $T\sim 330\text{ K}$ —a sensible value for the average gas temperature in this region. Knowing T_{gas} and the difference in path lengths $\Delta l=5\text{ cm}$, we can use the measured ΔLIA values and the appropriate $S(T=330\text{ K})$ line strength factor to estimate the average CH_4 number density in this region. The value so derived, $N_{CH_4}\sim 4.4\times 10^{16}\text{ cm}^{-3}$, matches well (to within 20%) with the ideal gas estimate at this T_{gas} , given the assumption that CH_4 is the only hydrocarbon present under these dilute carbon conditions. Equivalent calculations at higher carbon flow rates, and at all three z positions (1, 10.5, and 20.5 mm), return CH_4 and C_2H_2 number density estimates that agree well (to within factors of ~ 1.3 for CH_4 and ~ 2 for C_2H_2) with the corresponding $r=6\text{ cm}$ values reported in Ref. 5.

Figure 5 shows absorption spectra of activated (a) $CH_4/Ar/H_2$ and (b) $C_2H_2/Ar/H_2$ gas mixtures recorded in the narrow wavenumber range of $1274.1-1273.0\text{ cm}^{-1}$, which contains an isolated line associated with $C_2H_2, v=0, J=24$ molecules and a blended clump of lines around 1273.8 cm^{-1} . The absence of the 1273.262 cm^{-1} feature in spectra recorded at the lowest carbon flow rate accords with the conclusion (from Fig. 4) that any features evident in such spectra are likely attributable to CH_4 . Thus the very weak absorption evident at $\sim 1273.78\text{ cm}^{-1}$ in the $F(CH_4)=5\text{ SCCM}$ spectrum in Fig. 5(a) is most plausibly assigned to a cluster of blended lines associated with $CH_4(v=0)$ molecules in a highly excited ($J=19$) rotational level. Additional features are apparent at slightly higher wavenumber in spectra recorded at higher carbon flow rates. Inspection of Tables I and II reveal several potential contributors to this clump.

Two hot band absorptions associated with $\text{CH}_4(v_4=1)$ molecules lie in this range, with associated $S(T)$ factors that are comparable to that of the $4_0^1 P_{19}$ line once $T \sim 450$ K, but the clear showing of the 1273.262 cm^{-1} feature indicates that we need to consider possible contributions from C_2H_2 also—specifically the two $P(20)$ transitions at 1273.857 cm^{-1} (originating from the $4_1 5_1$ level) and at 1273.820 cm^{-1} (from the $v_5=1$ level). These two transitions have respective nuclear spin weightings of 3 and 1. At room temperature, the effect of the population difference far outweighs the different nuclear spin statistics, and the lower wavenumber line is dominant (see Fig. 3). Under base operating conditions, however, the two lines appear with similar LIAs—reflecting the convergence in relative populations of the two levels as T increases. As in Fig. 4, the C_2H_2 features are seen to grow in relative importance at higher carbon flow rates and, at a given carbon flow rate, to be consistently greater when using C_2H_2 as the source gas.

Figure 6 shows the calculated⁵ r dependence of the total number densities of CH_4 , C_2H_2 , C_2H_4 , and C_2H_6 and of T_{gas} for the standard process condition (25 SCCM CH_4 , 40 SCCM Ar, 500 SCCM H_2 , $p=150$ Torr, $P=1.5$ kW) at $z=0.5$ mm [Fig. 6(a)] and $z=10.5$ mm [Fig. 6(b)]. These clearly illustrate the way in which T_{gas} effects and gas phase chemistry combine to concentrate the stable hydrocarbon species in the cool regions at the periphery of the reactor. Even with the recessed windows, therefore, the measured LIAs will be dominated by gas at the ends of the probed column and any detailed comparison between experiment and model calculation requires that we give due consideration to the differences between the model and experimental geometries. Specifically, the probed column in configuration II extends to $r=7$ cm, and it is therefore necessary to extrapolate the model outputs for a further 1 cm. The recessed window mount is in good thermal contact with the reactor wall so, for the purpose of this exercise, we choose to retain the model predictions out to the largest calculated r value and assume that thereafter T declines linearly to 300 K at $r=7$ cm. We also assume that the mole fraction (X) of each species remains constant in the 1 cm extension region, but note that the model outputs actually show the mole fractions of all stable hydrocarbon species increasing by factors of 1.5–2 over the range of $5.5 < r < 6$ cm, presumably as a result of thermodiffusion effects. This allows estimation of n_{CH_4} , $n_{\text{C}_2\text{H}_2}$, T_{gas} , the relevant $S(T)$ factors, and thus the respective contributions to the total column absorption from each cell using a 1 mm grid spacing in the region of $6 < r < 7$ cm. Summing all contributions (modeled and extrapolated) from the range of $-7 < r < 7$ cm yields a calculated LIA for direct comparison with experimental measurements at the various process conditions.

The 2D model takes account of the changes in plasma parameters and conditions [e.g., T_{gas} , the electron temperature (T_e), and concentration (n_e), the power density and the plasma chemistry] induced by varying reactor parameters such as p , P , and the mole fractions of CH_4 and Ar in the process gas mixture. Detailed descriptions of this model procedure, which uses the plasma size as an external parameter, are presented in accompanying publications.^{5,20,23} By way of

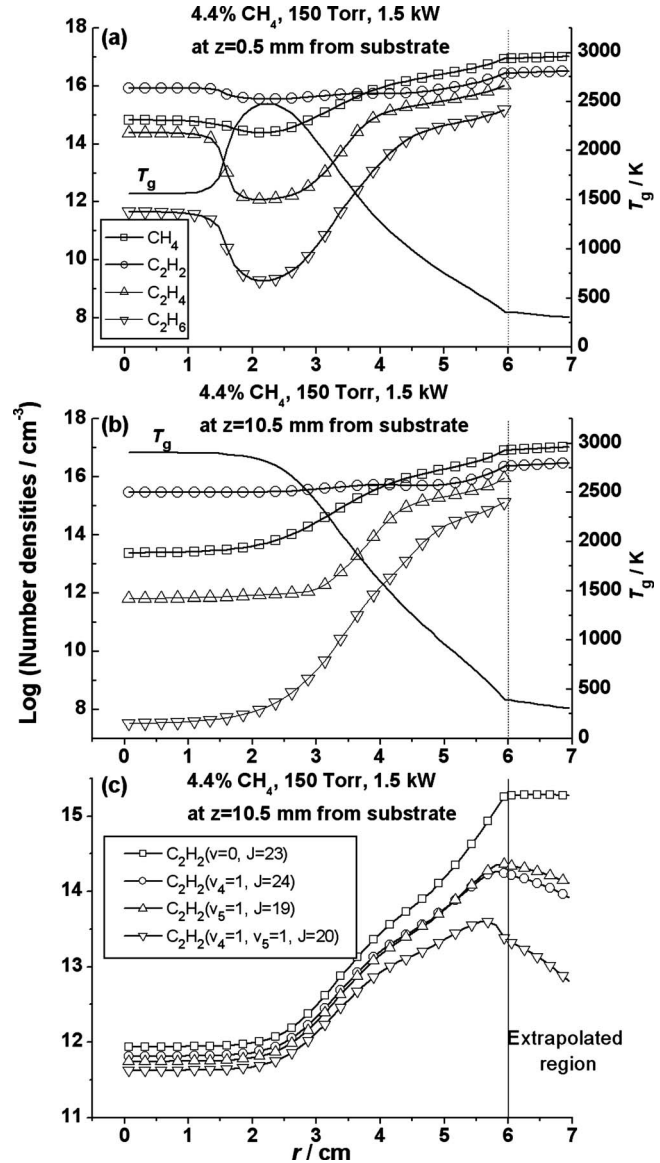


FIG. 6. Plots showing the r dependent CH_4 , C_2H_2 , C_2H_4 , and C_2H_6 number densities and T_{gas} values calculated for the standard process conditions [$F(\text{CH}_4)=25$ SCCM, $F(\text{Ar})=40$ SCCM, $F(\text{H}_2)=500$ SCCM, $p=150$ Torr, $P=1.5$ kW] at (a) $z=0.5$ mm and (b) $z=10.5$ mm. Panel (c) shows a decomposition of the calculated r dependent C_2H_2 total number density shown in (b) into number densities in the following quantum states: $v=0$, $J=23$; and individual ℓ -doublets of $v_5=1$, $J=20$; $v_4=1$, $J=24$; and $v_4=1+v_5=1$, $J=20$. Vertical dashed lines indicate the centers of gravity of the various state-specific number density distributions.

example, the maximal values of n_e and T_e are predicted to increase by $\sim 30\%$ and $\sim 5\%$, respectively, upon introducing just 5 SCCM of CH_4 (i.e., 0.88% CH_4) into an Ar/ H_2 plasma operating under what, otherwise, would constitute base conditions.^{5,23} Increasing the CH_4 flow rate further, up to the base value $F(\text{CH}_4)=25$ SCCM (i.e., 4.4% CH_4) leads to less pronounced changes in n_e (a further $\sim 5\%$ increase) and T_e [a $\sim 3\%$ decline relative to that at $F(\text{CH}_4)=5$ SCCM]. The 2D model returns the following typical values for the plasma parameters in the plasma core: $T_e \sim 1.25\text{--}1.45$ eV, $T_{\text{gas}} \sim 2800\text{--}2950$ K, power densities of $20\text{--}40 \text{ W cm}^{-3}$, reduced electric fields $E/N \sim 25\text{--}30$ Td, and $n_e \sim 3 \times 10^{11} \text{ cm}^{-3}$.^{5,20,23} The effects of heavy ($>90\%$) dilution of

TABLE III. Comparison of measured (exp) and predicted (mod) LIAs for the CH_4 $4_0^1 P5F_{12}$, C_2H_2 $4_0^1 5_0^1 P(23, e)$, and C_2H_2 $4_1^2 5_0^1 P(24, f)$ transitions as a function of process conditions.

Process conditions				CH_4 $4_0^1 P5F_{12}$		C_2H_2 $4_0^1 5_0^1 P(23, e)$		C_2H_2 $4_1^2 5_0^1 P(24, f)$	
$F(\text{CH}_4)$ (SCCM)	p (Torr)	P (kW)	d (mm)	LIA _{exp} (cm^{-1})	LIA _{mod} (cm^{-1})	LIA _{exp} (cm^{-1})	LIA _{mod} (cm^{-1})	LIA _{exp} (cm^{-1})	LIA _{mod} (cm^{-1})
25	150	1.50	1	0.0104	0.0088	0.0066	0.0024	0.000 96	0.000 27
25	150	1.50	11	0.0070	0.0076	0.0036	0.0020	0.000 48	0.000 21
25	150	1.50	21	0.0065	0.0085	0.0034	0.0019	0.000 34	0.000 21
5	150	1.50	11	0.0034	0.0030	0	0.0002	0	0.000 02
25	150	1.25	11	0.0081	0.0085	0.0040	0.0022	0.000 46	0.000 23
25	75	1.50	11	0.0026	0.0035	0.0026	0.0010	0.000 32	0.000 11

the process gas mixture by various noble gases (He, Ne, Ar, Kr) on both the plasma parameters and on nanocrystalline diamond deposition processes have also been investigated²⁴ experimentally and theoretically using the present 2D model for both Ar/H/C and He/H/C mixtures.

Table III compares the LIAs derived from such analyses of the 2D model outputs for the standard operating conditions (at three different z values) and for three alternative p , P , and $F(\text{CH}_4)$ conditions, with the corresponding values determined from measurements on the 1275.042 cm^{-1} line of $\text{CH}_4(v=0)$ and the 1275.512 cm^{-1} line of $\text{C}_2\text{H}_2(v=0)$. The model calculations reproduce the experimentally measured CH_4 LIAs rather well, under all process conditions, but consistently underestimate the corresponding experimental LIA value for C_2H_2 . Most of the C_2H_2 and, particularly, the CH_4 absorption is from gas at the periphery of the reactor.⁵ The $S(T)$ line strength factor for the $P(23)$ line used when monitoring $\text{C}_2\text{H}_2(v=0)$ molecules falls with decreasing T (for $T < 450 \text{ K}$), and we are unable to conceive of a physically plausible alternative $T_{\text{gas}}(r)$ dependence at large r that would allow the calculated $X_{\text{C}_2\text{H}_2}$ value to give a significantly larger absorbance. This leads us to suspect that the model calculation underestimates $X_{\text{C}_2\text{H}_2}$ in the cooler region of the viewing column. We can envisage two factors that may contribute to this underestimation. First, the predicted LIAs would be greater if $X_{\text{C}_2\text{H}_2}$ (and X_{CH_4}) increased through the region $6 < r < 7 \text{ cm}$, rather than remain constant (as currently assumed). Thermodiffusion considerations would favor the former scenario, but we see no robust way of predicting the necessary $X(r > 6 \text{ cm})$ dependences. Second, the present calculations return C_2H_4 and C_2H_6 number densities of $\sim 10^{16} \text{ cm}^{-3}$ at large r (see Fig. 6). It is quite possible that aspects of the gas phase chemical mechanism at large r or, more probably, the assumed gas-surface chemistry occurring at the reactor walls (that determines the interconversion between the various hydrocarbon species at low T_{gas} and thus the local C_2H_2 number density) needs further refinement.

Given local thermodynamic equilibrium, the partition functions calculated in the Appendix allow estimation of the fraction of $n_{\text{C}_2\text{H}_2}$ in any given v, J level at a given T . Figure 6(c) shows the relevant decomposition for probed levels highlighted in Figs. 4 and 5, namely, the $v=0, J=23$ level ($E''=649 \text{ cm}^{-1}$) and for individual ℓ -doublets of the $v_5=1, J=20$ ($E''=1225 \text{ cm}^{-1}$), $v_4=1, J=24$ ($E''=1318 \text{ cm}^{-1}$), and $v_4=1+v_5=1, J=20$ ($E''=1822 \text{ cm}^{-1}$) levels—plotted as a

function of r . As expected, the centers of gravity of the predicted state-specific number density distributions show a progressive shift to smaller r with increasing E'' ($\bar{r} \sim 6.5, 5.9, 5.8$, and 5.7 cm , respectively) but the effect is quite modest—emphasizing, once again, the localization of number density in the cooler periphery of the reactor. The last two columns in Table III compare LIAs for the unblended C_2H_2 $4_1^2 5_0^1 P(24, f)$ feature at 1274.156 cm^{-1} measured under a range of process conditions with those calculated using the predicted state-specific number density distributions and the appropriate $S(T)$ factors derived as outlined in the Appendix. Again, the experiment returns values that are consistently two or more times greater than the model calculations, with the greatest discrepancy at small z .

Figure 7 shows the LIAs for the CH_4 $4_0^1 4F_{23-5}F_{12}$, C_2H_2 $4_0^1 5_0^1 P(23, e)$ and C_2H_2 $4_1^2 5_0^1 P(24, f)$ transitions for (a) 25 SCCM $\text{CH}_4/40$ SCCM Ar/500 SCCM H_2 and (b) 12.5 SCCM $\text{C}_2\text{H}_2/40$ SCCM Ar/512.5 SCCM H_2 gas mixtures operating at standard conditions of total pressure and input power. The LIA of each of the monitored species is seen to decline with increasing z and, in each case, the hydrocarbon source gas shows relatively more strongly. Reference to Fig. 7 and to Table III suggests that the 2D model is rather successful in capturing the z dependence of the (absolute) CH_4 and (relative) C_2H_2 densities at large r .

C. Variation in CH_4 and C_2H_2 LIAs with process conditions

The upper two panels in Fig. 8 show the ways in which the LIAs for the same three probe transitions measured at $z = 11 \text{ mm}$ vary with input MW power under otherwise standard conditions; all three decline with increasing P , irrespective of whether the hydrocarbon source is provided by (a) $F(\text{CH}_4)=25$ SCCM or (b) $F(\text{C}_2\text{H}_2)=12.5$ SCCM. The lower two panels show corresponding measurements illustrating the effect of varying the total process gas pressure p while otherwise retaining standard process conditions of (c) $\text{CH}_4/\text{Ar}/\text{H}_2$ and (d) $\text{C}_2\text{H}_2/\text{Ar}/\text{H}_2$ mixing ratio, flow rate, and input MW power. The LIA of the source gas (CH_4) is always greatest in the former case, and the measured LIAs all increase roughly linearly with increasing p . In the case of the $\text{C}_2\text{H}_2/\text{Ar}/\text{H}_2$ input gas mixture, however, the LIAs of the $\text{C}_2\text{H}_2(v=0)$ and $\text{C}_2\text{H}_2(v_4=1)$ transitions both increase near linearly with p , while that for CH_4 rises much less steeply.

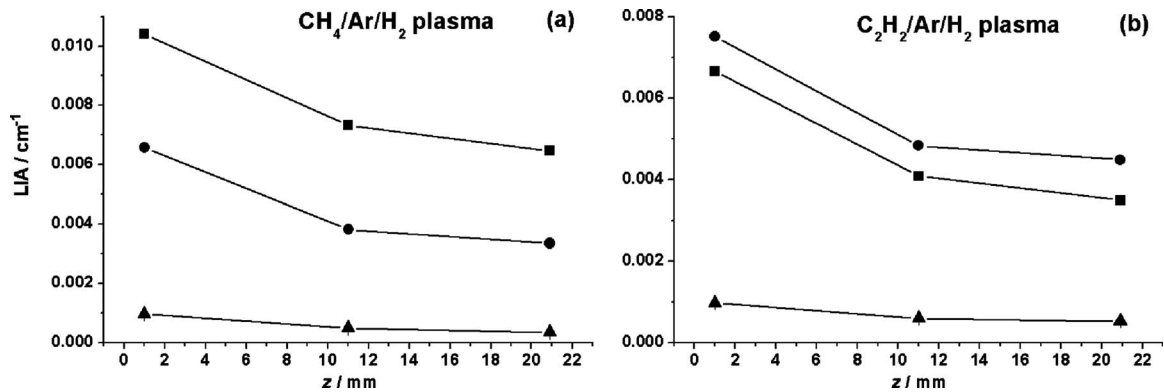


FIG. 7. Plots showing the z dependences of the LIAs for the CH₄ 4₀¹4F₂₃-5F₁₂ (■), C₂H₂ 4₀¹5₀¹P(23,e) (●) and C₂H₂ 4₁²5₀¹P(24,f) (▲) transitions measured for (a) $F(\text{CH}_4)=25$ SCCM, $F(\text{Ar})=40$ SCCM, $F(\text{H}_2)=500$ SCCM, and (b) $F(\text{C}_2\text{H}_2)=12.5$ SCCM, $F(\text{Ar})=40$ SCCM, $F(\text{H}_2)=512.5$ SCCM gas mixtures operating at standard conditions of total pressure and input power.

Reference to Table III shows, again, that the 2D model calculations for the standard CH₄/Ar/H₂ gas mixture captures the observed P and p dependences of the CH₄ LIAs quantitatively and the relative variation in the C₂H₂ LIAs.

The interpretation of these apparently simple trends requires consideration of several contributory factors. We start by considering the P variations and the case of a CH₄/Ar/H₂ gas mixture. The 2D model calculations for $P=1.25$ and 1.5 kW show that increasing P results in a slightly hotter, larger plasma region, some increase in T_{gas} at large r and a higher H atom density (n_{H}) throughout the reactor. The increase in T_{gas} leads to a steeper temperature (and thus total number density) gradient at large r , which has the effect of concentrating

more of the number density in the coolest periphery of the reactor and thus reducing the effective length of the column that contains most of the cold hydrocarbon gas. The LIA of all stable hydrocarbons thus declines with increasing P . Scrutiny of Fig. 8(a) shows that the decline in the C₂H₂ LIA is less steep than that for CH₄. Two factors contribute to this trend. First, higher P results in higher n_{H} and thus a greater processing efficiency of the input CH₄ (which is the source of the C₂H₂ under these conditions). Second, the $S(T)$ dependence of the 4₀¹5₀¹P(23,e) transition used to monitor C₂H₂($v=0$) molecules increases with T in the range of 300 < T < 450 K, so any increase in T_{gas} at large r as a result of

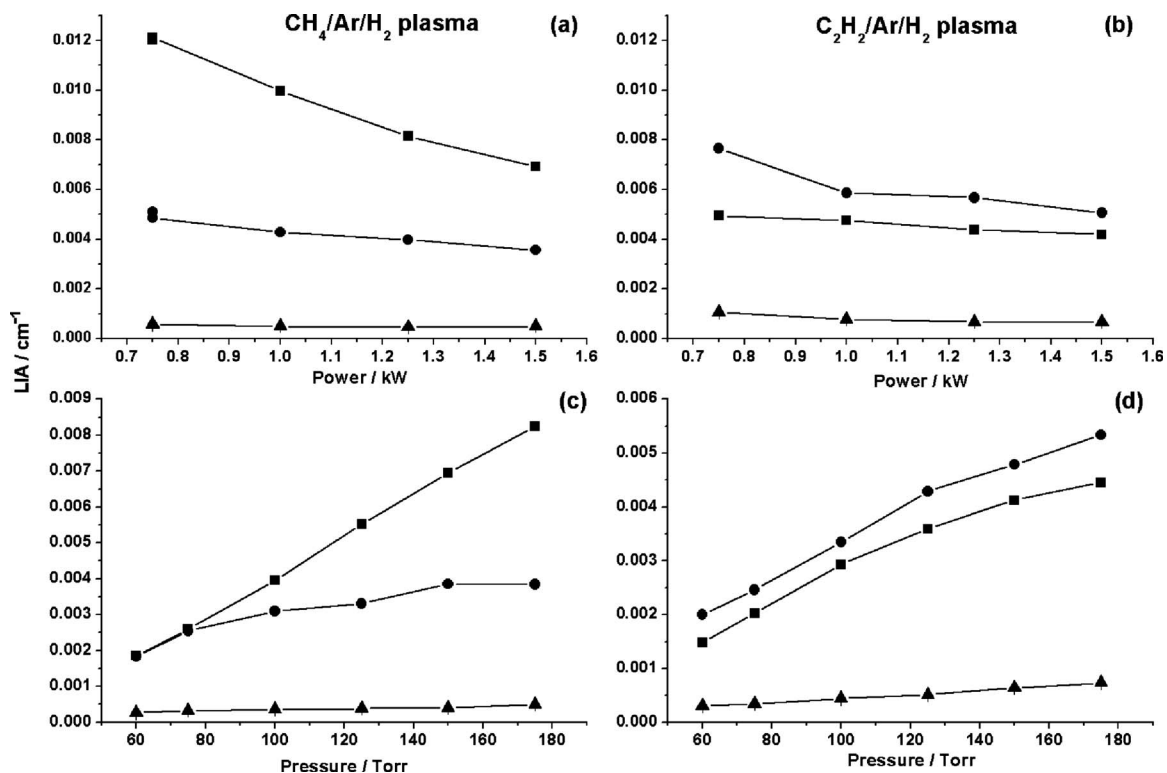


FIG. 8. Illustration of the P and p dependences of the LIAs for the CH₄ 4₀¹4F₂₃-5F₁₂ (■), C₂H₂ 4₀¹5₀¹P(23,e) (●), and C₂H₂ 4₁²5₀¹P(24,f) (▲) transitions measured at $z=11$ mm for 25 SCCM CH₄/40 SCCM Ar/500 SCCM H₂ [(a) and (c)] and 12.5 SCCM C₂H₂/40 SCCM Ar/512.5 SCCM H₂ [(b) and (d)] gas mixtures operating at standard conditions of total pressure [(a) and (b)] and input power [(c) and (d)]. The open symbols in (a) and (c) show the corresponding LIAs for the CH₄ 4₀¹4F₂₃-5F₁₂ and C₂H₂ 4₀¹5₀¹P(23,e) transitions returned by the 2D model calculations.

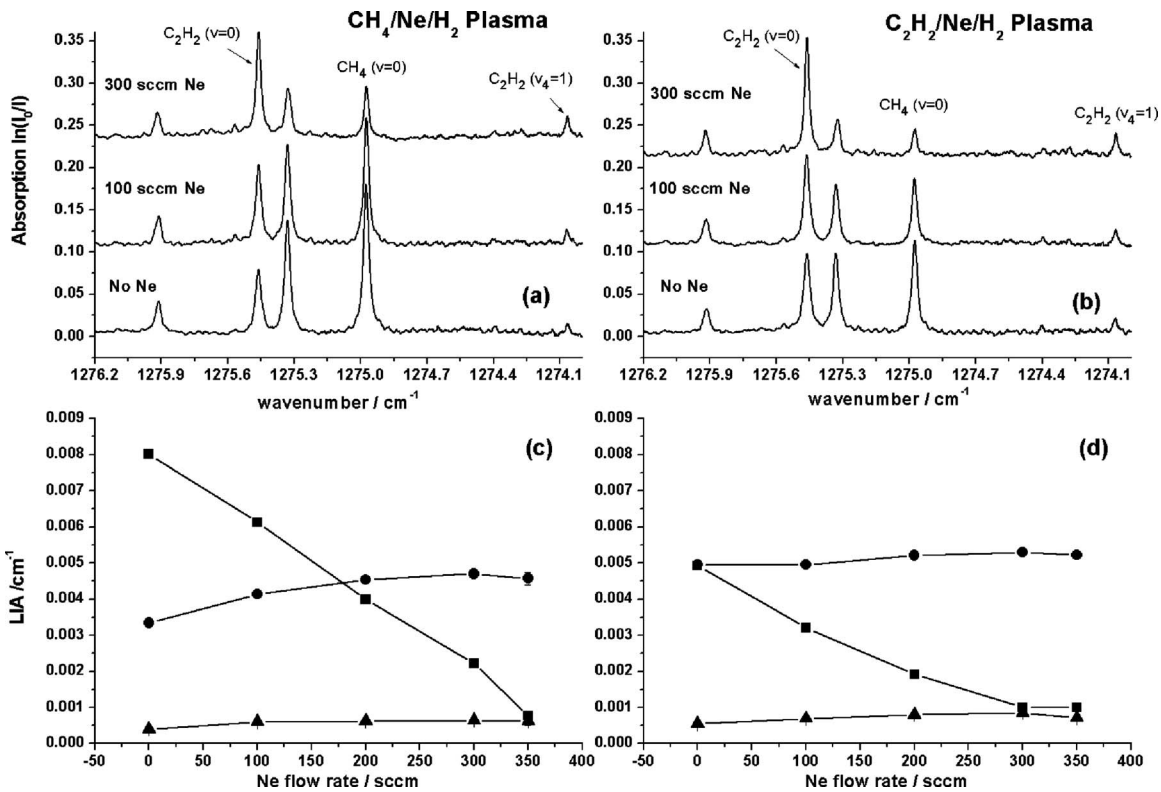


FIG. 9. Absorption spectra of activated (a) 25 SCCM CH₄/*x* SCCM Ne/(540−*x*)SCCM H₂ and (b) 12.5 SCCM CH₄/*x* SCCM Ne/(552.5−*x*)SCCM H₂ gas mixtures using three different Ne flow rates, recorded at *z*=11 mm over the wavenumber range of 1276.2–1274.0 cm⁻¹. Three unblended CH₄ and C₂H₂ features are labeled; detailed assignments of these transitions are given in Tables I and II. The total *p* (150 Torr) and *P* (1.5 kW) were the same for each of the spectra. (c) and (d) show the LIAs for the three unblended lines of interest and their variation with Ne flow rate.

increasing *P* will have a positive effect on the measured LIA. The data for the C₂H₂/Ar/H₂ gas mixture [Fig. 8(b)] display slightly different trends. In this case, the LIA of the source gas (C₂H₂) shows the steeper decline with increasing *P*. This can be understood if the main effect of increasing *P* is to increase *T*_{gas} and *n*_H and thus the extent of gas processing (by which the CH₄ is produced).

We now consider the observed variations in LIAs with *p*. The 2D model calculations for the standard CH₄/Ar/H₂ gas mixture show that doubling *p* from 75 Torr to (the standard) 150 Torr results in an approximately fourfold increase in *n*_H at the center of the plasma ball (equivalent to an approximately twofold increase in the H atom mole fraction), but a ~50-fold drop in *n*_H (from ~3 × 10¹⁰ to ~6 × 10⁸ cm⁻³) at *r*=6 cm. The same calculations show little change in *T*_{gas} at *r*=6 cm as a result of this increase in *p*. The reduction in *n*_H at large *r* is mainly attributable to the *p*⁻¹ dependence of the diffusion coefficients and thus the H atom diffusional transfer rate from the source region (the plasma ball), but will be exacerbated by the increased opportunity for reactive loss through reaction with hydrocarbon species at higher *p*. This latter point may be significant in explaining the *p* dependence of the LIAs measured with the C₂H₂/Ar/H₂ gas mixture. In this case, the LIA of the source hydrocarbon (in both its *v*=0 and *v*₄=1 levels) increases roughly linearly with *p*, as expected, but that for CH₄ grows more slowly at higher *p*. All of the CH₄ in this mixture is formed by reactions involving H atoms, principally in regions of moderate *T*_{gas}. The reduction in *n*_H at large *r* at high *p* will lead to a reduction in

C₂H₂ → CH₄ conversion probability in the peripheral regions (where most of the monitored CH₄ is located), thus accounting for the observed negative curvature in the CH₄ LIA at the highest *p* studied.

Similar considerations can account for the observed variations in the LIAs for the same three probe transitions when varying the Ar/H₂ (or Ne/H₂) ratio in CH₄/Ar(Ne)/H₂ and C₂H₂/Ar(Ne)/H₂ gas mixtures. Figures 9(a) and 9(b) show sample absorption spectra measured at *z*=11 mm for CH₄/Ne/H₂ and C₂H₂/Ne/H₂ gas mixtures. The carbon and total flow rates were the same in all cases (25 and 565 SCCM, respectively), as were *p* (150 Torr) and *P* (1.5 kW), with the only variable being the Ne/H₂ ratio. Figures 9(c) and 9(d) show how the LIAs for the three unblended lines of interest vary with Ne flow rate. Equivalent measurements involving CH₄/Ar/H₂ and C₂H₂/Ar/H₂ gas mixtures return virtually identical LIA versus *F*(Ar) plots. The most striking feature of these plots is the very different behavior of the C₂H₂ and CH₄ LIAs; the former are relatively insensitive to the Ne/H₂ ratio (or actually increase in the case that CH₄ is the source gas), whereas the CH₄ LIA falls more than fivefold over the investigated range of Ne flow rates—with the result that the strongest absorption at high *F*(Ne) is due to C₂H₂(*v*=0) molecules. Indeed, in the case of the C₂H₂/Ne/H₂ gas mixture, vibrationally hot C₂H₂(*v*₅=1) molecules contribute ~50% of the LIA of the blended feature at ~1275.3 cm⁻¹, with the result that it actually appears more intense than the neighboring CH₄(*v*=0) feature at 1275.04 cm⁻¹. This should be contrasted with the

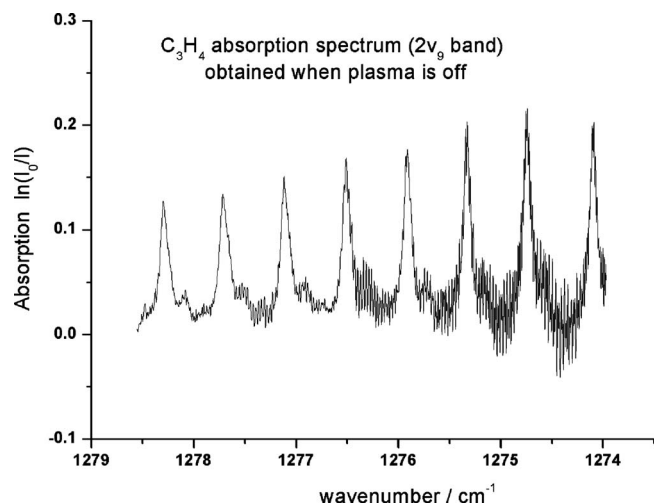


FIG. 10. Part of the 9_0^2 absorption band of a 5 Torr room temperature sample of propyne.

spectrum obtained with the 2.5 SCCM C_2H_2 /40 SCCM Ar/522.5 SCCM H_2 gas mixture [Fig. 4(b)], which is dominated by CH_4 absorptions and the higher frequency of these two lines is just 2/3 as intense as the 1275.04 cm^{-1} feature [consistent with the respective lower state degeneracies (see Table I)]. The rationale for the present observations is similar to that used to explain the observed p dependent variations in LIA. Substituting H_2 with rare gas (Ne or Ar) reduces the thermal conductivity of the gas, resulting in an increase in T_{gas} in the plasma region. This facilitates $CH_4 \rightarrow C_2H_2$ conversion in the hotter regions and explains the increase in C_2H_2 LIA with increasing $F(Ne)$ in Fig. 9(c). Increased T_{gas} in the plasma region will encourage H_2 dissociation (and thus an increase in n_H), but such increases will be countered by the reduction in $F(H_2)$. As in the case of increasing p , therefore, we can anticipate that increasing $F(Ne)$ will result in a progressive decrease in n_H at larger r and thus a reduced probability for CH_4 formation via reaction (3) in the cooler regions of the reactor—consistent with the observed decline in CH_4 LIA.

D. Use of other hydrocarbon feedstock gases

Four other hydrocarbon source gases (ethane, propyne, n -propane, and n -butane) were investigated in addition to CH_4 and C_2H_2 ; all were found to show broadly similar behavior. The scan range of the QC laser spans part of the 9_0^2 absorption band of propyne, as illustrated by the spectrum of a 5 Torr room temperature sample of propyne shown in Fig. 10. This absorption is also clearly evident in spectra of 8.3 SCCM propyne/40 SCCM Ar/516.7 SCCM H_2 gas samples at room temperature and $p=150$ Torr, but completely disappears once the plasma is ignited—to be replaced by the familiar absorption lines of CH_4 and C_2H_2 . Figures 11(a)–11(d) show LIAs for the standard probe transitions for $CH_4(v=0)$ and $C_2H_2(v=0)$ measured with these four alternative hydrocarbons under otherwise standard conditions at $z=11$ mm plotted as a function of carbon flow rate $F(C)$. The quoted flow rates rely on use of the manufacturer correction factors (where available) and may not be as reliable

as those quoted previously for CH_4 and C_2H_2 . Nonetheless, a number of common trends are readily apparent—that are very reminiscent of those observed when using C_2H_2 as the source gas [Fig. 4(d)]. In all cases, the dominant LIA at low carbon flow rate is associated with CH_4 , but this LIA stops increasing once $F(C) \sim 15$ SCCM. The LIAs of the transitions used to monitor C_2H_2 in its $v=0$ and $v_4=1$ levels both increase with $F(C)$. Notwithstanding the caveat regarding the accuracies of the quoted carbon flow rates, there is a notable and consistent difference at high $F(C)$ between the upper plots (involving unsaturated hydrocarbon source gases) and the lower plots (involving alkanes); in the former cases, the C_2H_2 LIA has actually grown to exceed the CH_4 LIA. This may well be a real effect, since the choice of hydrocarbon affects the overall C/H ratio. In the case of a 40 SCCM CH_4 /40 SCCM Ar/485 SCCM H_2 flow, for example, the overall C/H ratio in the input gas mixture is $40/1130=0.0354$. Use of C_3H_8 or C_4H_{10} at the same carbon flow rate [i.e., 10 SCCM in the case of C_4H_{10} , with $F(H_2)$ raised to 515 SCCM to conserve the same F_{total}] gives the same input C/H ratio. For the unsaturated hydrocarbons, however, the input C/H ratio will necessarily be higher. For example, the equivalent calculation for $F(propyne) = 13.33$ SCCM [and $F(H_2) = 511.67$ SCCM] yields an input C/H ratio of 0.0372. Figures 11(e) and 11(f) show, respectively, the LIAs for the probed $CH_4(v=0)$ and $C_2H_2(v=0)$ probe transitions for these four source gases plotted on a common C/H ratio scale. The detailed explanation of such trends is again guided by the 2D modeling results, but is reserved pending description of the time evolution of the LIAs of interest following introduction of both CH_4 and C_2H_2 into a pre-existing Ar/ H_2 plasma.

E. Time dependence of the LIAs following addition of $CH_4(C_2H_2)$ to a pre-existing Ar/ H_2 plasma

The fast spectral acquisition rate achievable with the chirped QC laser allows study of the way in which the various LIAs approach their asymptotic values following introduction of a hydrocarbon flow to a pre-existing Ar/ H_2 plasma. Figure 12 shows illustrative spectra recorded at different times after the addition of (a) $F(CH_4)=25$ SCCM and (b) $F(C_2H_2)=12.5$ SCCM to an Ar/ H_2 plasma operating with $F(Ar)=40$ SCCM, $F(H_2)$ appropriate to ensure that the asymptotic $F_{total}=565$ SCCM, $p=150$ Torr, and $P=1.5$ kW. As noted previously,¹⁶ the unblended (and the blended) $CH_4(v=0)$ features appear at earliest time, even when using C_2H_2 as the source gas. As shown in Figs. 12(c) and 12(d), the $C_2H_2(v=0)$ and $C_2H_2(v_4=1)$ absorption features appear later (as do features associated with the $v_5=1$ level of C_2H_2) and take longer to attain their asymptotic LIA values. Such data provide a further—in this case, time-dependent—illustration of the effect of varying the C/H ratio. Qualitatively at least, the data display all of the same trends as noted previously. At low C/H ratio (early time in these experiments) the main hydrocarbon detected is CH_4 , but C_2H_2 LIAs grow in relative intensity at later time (higher C/H ratio).

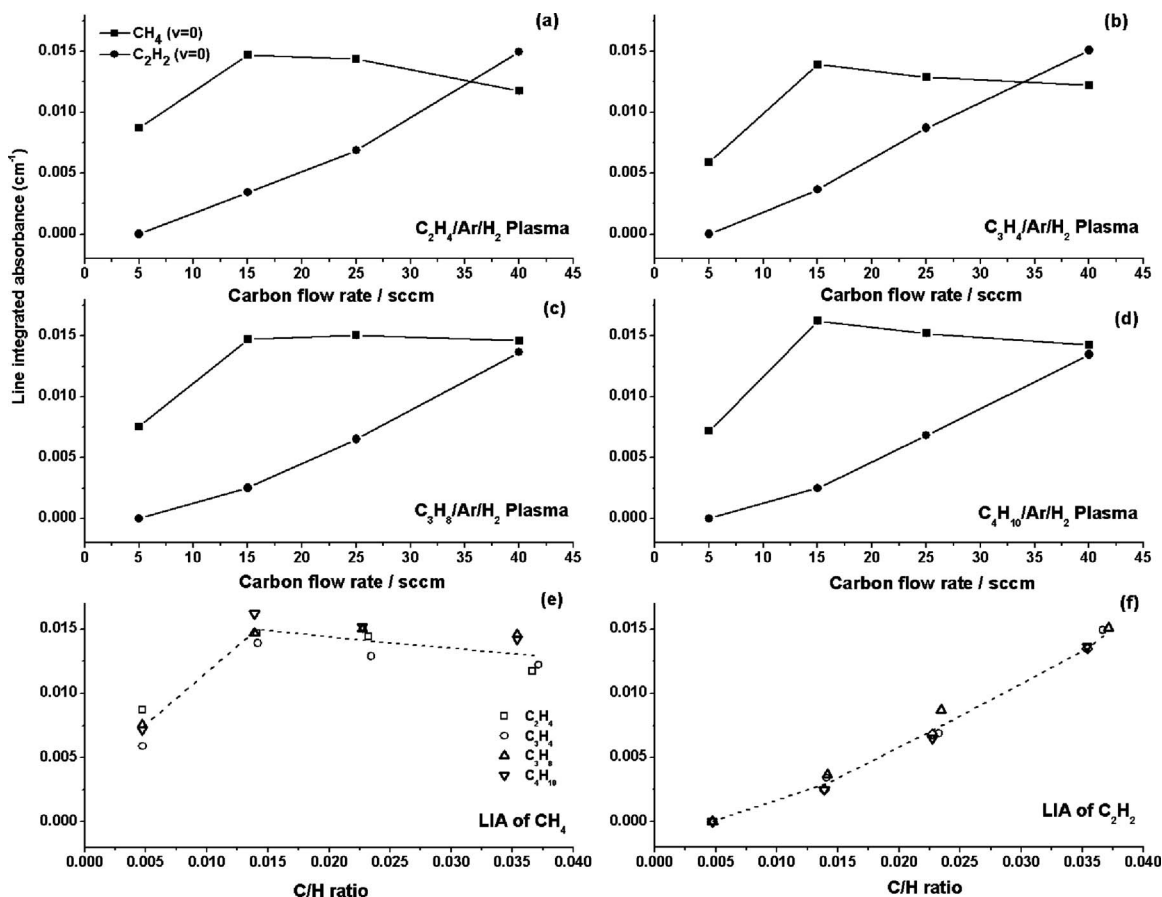


FIG. 11. LIAs for the standard probe transitions of CH₄($v=0$) and C₂H₂($v=0$) measured at $z=11$ mm in four different hydrocarbon/Ar/H₂ gas mixtures at $p=150$ Torr and $P=1.5$ kW, as a function of carbon flow rate: (a) ethane, (b) propyne, (c) *n*-propane, and (d) *n*-butane. $F(\text{Ar})$ and F_{total} were maintained constant at, respectively, 40 and 565 SCCM throughout, and $F(\text{H}_2)$ adjusted to compensate as $F(\text{hydrocarbon})$ was varied. The CH₄($v=0$) and C₂H₂($v=0$) LIA data for these four molecules are plotted on a common C/H ratio scale in panels (e) and (f), respectively.

F. Mechanism of CH₄ ↔ C₂H₂ interconversion and its spatial dependence

Figure 13 displays (production-loss) rates of H atoms, CH₄, C₂H₂, and C₂H₄ plotted as a function of z at $r=0$ returned by the 2D model calculations for standard process conditions: i.e., 25 SCCM CH₄, 40 SCCM Ar, 500 SCCM H₂, $p=150$ Torr, $P=1.5$ kW. The z dependence of these calculated (production-loss) rate profiles are relatively unaffected by reducing $F(\text{CH}_4)$ to 5 SCCM or p to 75 Torr, although both such changes reduce the respective magnitudes of the rates. To a reasonable approximation, these profiles are radially symmetric in the r, z space above the substrate. As noted in Ref. 5 inspection of such figures encourages discussion of the reactor volume in terms of three concentric volumes: **A**, the plasma region (that is located directly above the substrate, contains the highest T_{gas} and is characterized by large H atom production rates); **B**, an annular shell characterized by $1400 < T_{\text{gas}} < 2200$ K, efficient conversion of CH₄ (and C₂H₄) into C₂H₂ and the consumption of H atoms required for this conversion; and **C**, the cooler outer region ($T_{\text{gas}} < 1400$ K) characterized by net conversion of C₂H₂ into CH₄ (and C₂H₄) and low H atom consumption rates. Tables IV and V summarize the more important reaction sequences (i.e., those involving elementary steps with calculated rates $> 10^{17}$ cm⁻³ s⁻¹) that drive

these transformations in the centers of region **B** ($z=3.5$ cm, where $T_{\text{gas}} \sim 1900$ K) and region **C** ($z=4.8$ cm, where $T_{\text{gas}} \sim 1100$ K). Several of the elementary steps in the CH₄ → C₂H₂ conversion scheme shown in Table IV consume H atoms—consistent with the substantial calculated H atom loss rate in region **B** ($\sim 4 \times 10^{16}$ cm⁻³ s⁻¹). The calculated H atom (production-loss) rate in region **C**, in contrast, is small—consistent with the reduced mechanism listed in Table V. H atoms are needed to drive C₂H₂ → CH₄ conversion in region **C**, but they are not (substantially) consumed by this conversion.

Such 2D model outputs provide a rationale for all of the trends observed experimentally. Under standard process conditions, CH₄ or C₂H₂ feedstock gas is converted into a mixture containing both of these hydrocarbons (Fig. 4). The full 2D modeling predicts the presence of other stable hydrocarbons also (C₂H₄, C₂H₆, etc.) at lower mole fraction, but the tuning range of the available QC laser precludes the possibility of observing these species. Thermodiffusion drives the stable hydrocarbon species toward regions of lower T_{gas} but chemical processing is occurring in parallel—driving net CH₄ ↔ C₂H₂ interconversion forward in region **B** and backward in region **C**. The gas composition in the outermost parts of the reactor may be further complicated by wall reactions and the effects of local stagnation volumes, which are prob-

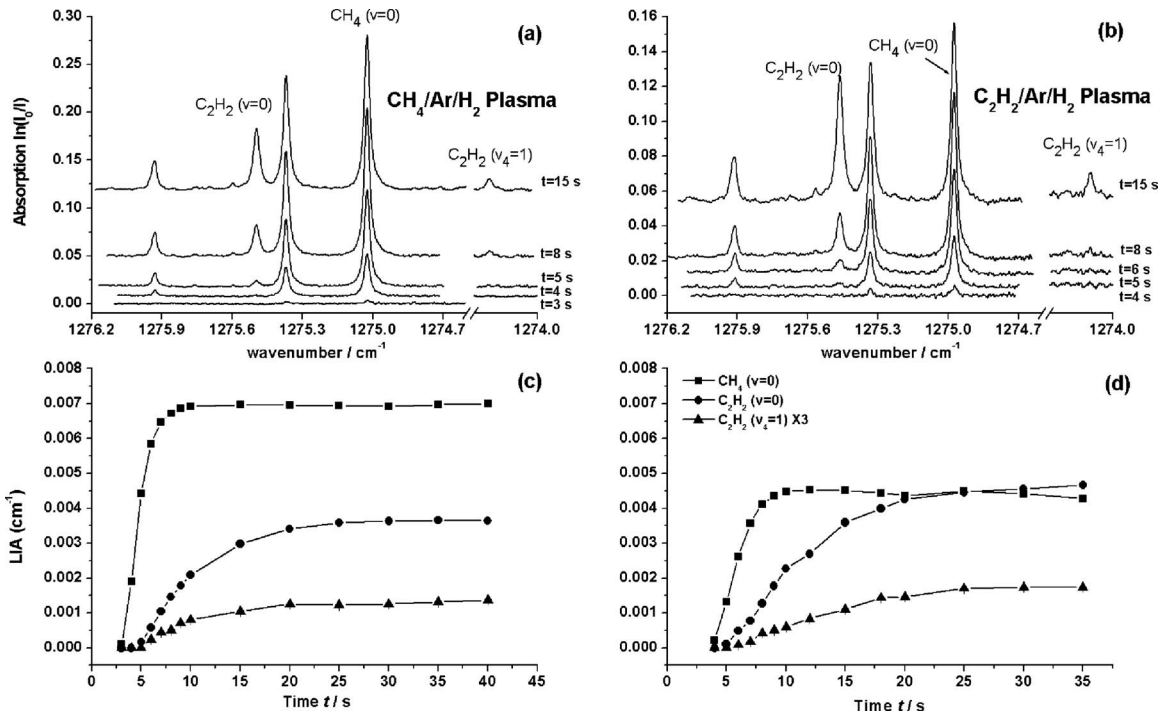


FIG. 12. Absorption spectra recorded at $z=11$ mm at different times t after addition of (a) $F(\text{CH}_4)=25$ SCCM and (b) $F(\text{C}_2\text{H}_2)=12.5$ SCCM to an Ar/H₂ plasma operating with $F(\text{Ar})=40$ SCCM, $F(\text{H}_2)$ appropriate to ensure that the asymptotic $F_{\text{total}}=565$ SCCM, $p=150$ Torr and $P=1.5$ kW. Plots (c) and (d) show the growth of the LIAs for the standard CH₄($\nu=0$), C₂H₂($\nu=0$), and C₂H₂($\nu_4=1$) probe transitions as a function of time after switching on the hydrocarbon MFC (which defines $t=0$).

ably not treated well in the model calculations. The gas composition in this region may be further complicated by transport of (unprocessed) source gas—the LIAs shown in Figs. 4(c) and 4(d) clearly indicate a relative excess of the respective source gas at higher carbon flow rates. The number density profiles (dictated by T_{gas}) and $S(T)$ line strength factors mean that the present QC laser measurements studies (and any other line-of-sight IR studies of stable hydrocarbon species in such reactors) are necessarily heavily biased toward material in region C—the cold periphery of the reactor (recall Fig. 6). Even when using recessed windows (configuration II), therefore, gas in the hot plasma region (A) makes no

direct contribution to the measured LIAs. As Fig. 11 shows, all of the alternative hydrocarbon source gases investigated are processed, efficiently, to similar CH₄/C₂H₂ mixtures.

The time dependent studies (Fig. 12) provide a particularly clear illustration of the role of region C. At $t=0$, this region contains just Ar, H₂, and H atoms. Upon adding CH₄ (or any other hydrocarbon) through inlets sited at the top of the reactor, the shortest diffusion path is directly downwards—i.e., transport localized in the outer region (C). As Table V shows, CH₄ is the most stable hydrocarbon in this region. Hence the dominance of the CH₄ features at early t —irrespective of the choice of input hydrocarbon. The input carbon must traverse a longer path in order for C₂H₂ to build up in the viewing column within region C—from the gas inlets, through C, into B [where the requisite CH₄ → C₂H₂ occurs (Table IV)], and then radially outward again into the cooler part of the viewing column. This longer diffusional path is reflected by the longer observed buildup time for the C₂H₂ LIA (Fig. 12). The efficiency of C₂H₂ → CH₄ processing in region C depends on the local C/H ratio. In the time dependent studies, this ratio increases with t until reaching the asymptotic value appropriate to the chosen process conditions.

Finally we revisit the results of the steady state experiments in the context of the above discussion. At low carbon flow rates [$F(\text{C})=5$ SCCM], the C/H ratio in region C is sufficiently low that all hydrocarbon species in this region are processed to CH₄—consistent with the dominance of CH₄ features in the absorption spectra measured under these conditions (Figs. 4 and 11). Increasing $F(\text{C})$ leads to a progressive increase in the C/H ratio in region C and in the

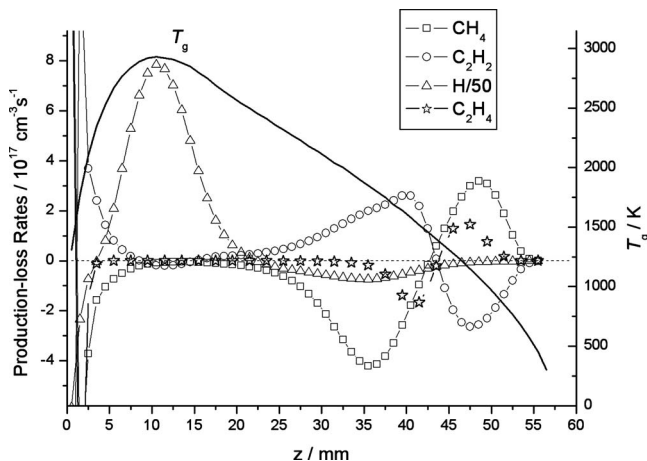


FIG. 13. Calculated (production-loss) rates of H atoms, CH₄, C₂H₂, and C₂H₄ (and T_{gas}) plotted as functions of z at $r=0$ for standard process conditions: i.e., $F(\text{CH}_4)=25$ SCCM, $F(\text{Ar})=40$ SCCM, $F(\text{H}_2)=500$ SCCM, $p=150$ Torr, $P=1.5$ kW.

TABLE IV. Simplified $\text{CH}_4 \rightarrow \text{C}_2\text{H}_2$ conversion mechanism highlighting key elementary reactions with rates $>10^{17} \text{ cm}^{-3} \text{ s}^{-1}$ under standard process conditions at $z=3.5 \text{ cm}$ (i.e., region **B**), where $T_{\text{gas}} \sim 1900 \text{ K}$.

	Reaction	Reaction rate $/(\text{cm}^{-3} \text{ s}^{-1})$	Net conversion; net rate $/(\text{cm}^{-3} \text{ s}^{-1})$
1	$\text{CH}_4 + \text{H} \rightarrow \text{CH}_3 + \text{H}_2$	7.28×10^{19}	$\text{CH}_4 \rightarrow \text{CH}_3$; 2.5×10^{17}
2	$\text{CH}_3 + \text{H}_2 \rightarrow \text{CH}_4 + \text{H}$	7.14×10^{19}	
3	$\text{CH}_3 + \text{H}(\text{+M}) \leftrightarrow \text{CH}_4(\text{+M})$	1.20×10^{18}	
4	$\text{CH}_3 + \text{H} \rightarrow {}^1\text{CH}_2 + \text{H}_2$	5.24×10^{18}	$\text{CH}_3 \rightarrow {}^1/3\text{CH}_2$; 1.6×10^{17}
5	${}^1\text{CH}_2 + \text{H}_2 \rightarrow \text{CH}_3 + \text{H}$	5.11×10^{18}	
6	${}^3\text{CH}_2 + \text{H}_2 \rightarrow \text{CH}_3 + \text{H}$	2.97×10^{17}	
7	$\text{CH}_3 + \text{H} \rightarrow {}^3\text{CH}_2 + \text{H}_2$	3.27×10^{17}	
8	${}^1\text{CH}_2(\text{+M}) \rightarrow {}^3\text{CH}_2(\text{+M})$	1.89×10^{18}	${}^1\text{CH}_2 \rightarrow {}^3\text{CH}_2$; 1.3×10^{17}
9	${}^3\text{CH}_2(\text{+M}) \rightarrow {}^1\text{CH}_2(\text{+M})$	1.76×10^{18}	
10	${}^3\text{CH}_2 + \text{CH}_4 \rightarrow \text{C}_2\text{H}_4 + \text{H}_2$	1.35×10^{17}	$\text{CH}_x + \text{CH}_y \rightarrow \text{C}_2\text{H}_4$; 1.35×10^{17}
11	$\text{C}_2\text{H}_4 + \text{H} \rightarrow \text{C}_2\text{H}_3 + \text{H}_2$	1.53×10^{18}	$\text{C}_2\text{H}_4 \rightarrow \text{C}_2\text{H}_3$; 2.1×10^{17}
12	$\text{C}_2\text{H}_3 + \text{H}_2 \rightarrow \text{C}_2\text{H}_4 + \text{H}$	1.32×10^{18}	
13	$\text{C}_2\text{H}_3 + \text{H} \rightarrow \text{C}_2\text{H}_2 + \text{H}_2$	2.36×10^{17}	$\text{C}_2\text{H}_3 \rightarrow \text{C}_2\text{H}_2$; 2.1×10^{17}
14	$\text{C}_2\text{H}_3(\text{+M}) \rightarrow \text{C}_2\text{H}_2 + \text{H}(\text{+M})$	7.14×10^{17}	
15	$\text{C}_2\text{H}_2 + \text{H}(\text{+M}) \rightarrow \text{C}_2\text{H}_3(\text{+M})$	7.40×10^{17}	

$\text{C}_2\text{H}_2/\text{CH}_4$ ratio in region **B**. Diffusive transport ensures that the steady state C_2H_2 density in region **C** thus increases also—to levels that are easily detectable in the single pass line-of-sight IR absorption spectrum. As already discussed (Sec. III C), increasing p (at constant input mixing ratio) or substituting part of $F(\text{H}_2)$ with Ar (or Ne) has the effect of reducing n_{H} in region **C**, thereby reducing the probability of $\text{C}_2\text{H}_2 \rightarrow \text{CH}_4$ conversion in this region and increasing the relative showing of C_2H_2 (as compared with CH_4) in the line-of-sight IR absorption spectrum.

IV. CONCLUSION

The QCL measurements reported here serve to highlight many of the strengths and the limitations of applying line-of-sight absorption methods to stable gas phase species in a reactor containing very large temperature (and number density) gradients. The principle limitation is that the measured absorptions are associated with molecules in the cool periphery of the reactor (**C**); the present measurements provide no direct measure of molecules in the central plasma region (**A**)

TABLE V. Simplified $\text{C}_2\text{H}_2 \rightarrow \text{CH}_4$ conversion mechanism highlighting key elementary reactions with rates $>10^{17} \text{ cm}^{-3} \text{ s}^{-1}$ under standard process conditions at $z=4.8 \text{ cm}$ (i.e., region **C**), where $T_{\text{gas}} \sim 1100 \text{ K}$.

	Reaction	Reaction rate $/(\text{cm}^{-3} \text{ s}^{-1})$	Net conversion; net rate $/(\text{cm}^{-3} \text{ s}^{-1})$
1	$\text{C}_2\text{H}_2 + \text{H}(\text{+M}) \rightarrow \text{C}_2\text{H}_3(\text{+M})$	2.32×10^{17}	$\text{C}_2\text{H}_2 \rightarrow \text{C}_2\text{H}_3$; 2.1×10^{17}
2	$\text{C}_2\text{H}_3 + \text{H}_2 \rightarrow \text{C}_2\text{H}_4 + \text{H}$	2.78×10^{17}	$\text{C}_2\text{H}_3 \rightarrow \text{C}_2\text{H}_4$; 2.1×10^{17}
3	$\text{C}_2\text{H}_4 + \text{H}(\text{+M}) \rightarrow \text{C}_2\text{H}_5(\text{+M})$	1.54×10^{17}	$\text{C}_2\text{H}_4 \rightarrow \text{C}_2\text{H}_5$; 1.3×10^{17}
4	$\text{C}_2\text{H}_5 + \text{H} \rightarrow \text{CH}_3 + \text{CH}_3$	1.42×10^{17}	$\text{C}_2\text{H}_5 \rightarrow 2\text{CH}_3$; 1.4×10^{17}
5	$\text{CH}_3 + \text{H}_2 \rightarrow \text{CH}_4 + \text{H}$	1.00×10^{18}	$\text{CH}_3 \rightarrow \text{CH}_4$; 2.1×10^{17}
6	$\text{CH}_4 + \text{H} \rightarrow \text{CH}_3 + \text{H}_2$	7.93×10^{17}	

from whence diamond growth occurs. Notwithstanding, they are hugely informative with regards to gas processing within the reactor, and to testing, tensioning and refining the companion 2D model calculations. The present studies show that any chosen hydrocarbon source gas will be converted into a mixture dominated by CH_4 and C_2H_2 , and that the continuing interconversion between these two species depends sensitively on both T_{gas} and n_{H} , and thus on process conditions (pressure, input power, input gas mixing ratios, etc.) and location within the reactor. $\text{CH}_4 \rightarrow \text{C}_2\text{H}_2$ conversion occurs most efficiently in regions characterized by $1400 < T_{\text{gas}} < 2200 \text{ K}$, which correlate with an annular shell (region **B**) around the central plasma (region **A**), whereas the reverse transformation $\text{C}_2\text{H}_2 \rightarrow \text{CH}_4$ is favored in the outermost region (**C**) where $T_{\text{gas}} < 1400 \text{ K}$.

ACKNOWLEDGMENTS

The Bristol group is grateful to EPSRC for the award of a portfolio grant (LASER), to Element Six Ltd for financial support and the long term loan of the MW reactor, to the University of Bristol and the Overseas Research Scholarship (ORS) scheme for a postgraduate scholarship (J.M.), and to colleagues J. J. Henney, K. N. Rosser and Dr. C. M. Western and Dr. J. A. Smith for their many contributions to the work described here. The Strathclyde group is grateful to EPSRC for funding the initial part of their QC laser spectrometer development program and for a research studentship (to K.G.H.), to NERC for funding subsequent QC laser spectrometer development, and to the Leverhulme Trust for the award of an Emeritus Fellowship (to G.D.). Y.A.M. is pleased to acknowledge support from RF Government for Key Science Schools Grant No. 133.2008.2. The collaboration between Bristol and Moscow is supported by a Royal Society Joint Project Grant.

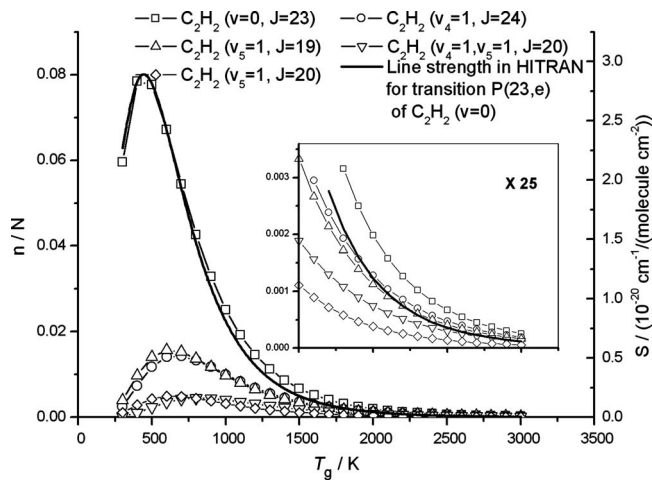


FIG. 14. Plot showing the calculated T dependence of n/N [Eq. (A1)] for selected C_2H_2 levels of interest: $v=0$, $J=23$ ($E''=649$ cm^{-1} , \blacksquare); $v_5=1$, $J=19$ ($E''=1177$ cm^{-1} , \triangle); $v_5=1$, $J=20$ ($E''=1225$ cm^{-1} , \diamond); $v_4=1$, $J=24$ ($E''=1319$ cm^{-1} , \circ); and $v_4=1+v_5=1$, $J=20$ ($E''=1822$ cm^{-1} , ∇). Also shown (solid curve and right hand scale) is the $S(T)$ line strength factor for the $4_0^1 5_0^1 P(23)$ transition from HITRAN (Ref. 21). The two vertical axes have been scaled to highlight the analogous T dependences and to establish the best-fit scaling factor linking n and S . The inset shows the various n/N values at high T on an expanded (25 times) vertical scale.

APPENDIX

The estimation of $S(T)$ line strengths for transitions from vibrationally excited levels of C_2H_2 involves calculation of the internal (vibration and rotation) partition function in the rigid rotor, harmonic oscillator limit using analytical formulas as outlined by Herzberg.²⁶ Such an approach is justified in the present context given the small size of the rotational constant ($B=1.1766$ cm^{-1}) relative to the T_{gas} values of interest. In this limit, the fraction of the total population in any given level m with energy E_m is given by

$$\frac{n_m}{N} = \frac{g_m \exp(-E_m/kT)}{Q_{int}}, \quad (A1)$$

where g_m incorporates the rotational $(2J+1)$ and nuclear spin (3 or 1, for ortho- and para-levels, respectively) degeneracies. Q_{int} is the internal (rotation, vibration) partition function, given by

$$Q_{int} = \frac{(kT/\sigma hcB)}{\prod_i [1 - \exp(-\omega_i hc/kT)]^{d_i}}, \quad (A2)$$

where ω_i is the wavenumber of fundamental vibration i with degeneracy d_i , the product in the denominator runs over the five fundamental modes of vibration, and σ is the symmetry factor (2 in the case of C_2H_2).

Figure 14 shows the calculated T dependence of n/N [Eq. (A1)] for the following levels of C_2H_2 : $v=0$, $J=23$ (which shows much the strongest absorption in this spectral region); $v_5=1$, $J=20$ ($E''=1225$ cm^{-1}); $v_4=1$, $J=24$ ($E''=1319$ cm^{-1}); and $v_4=1+v_5=1$, $J=20$ ($E''=1822$ cm^{-1}). As noted earlier (Sec. III B), the two $J=20$ levels have different nuclear spin statistical weights. Also shown (right hand axis) is the $S(T)$ curve for the $4_0^1 5_0^1 P(23)$ transition.²¹ The two vertical axes have been scaled to highlight the (expected) reasonable match between the respective T dependences,

thereby demonstrating that the above approach offers a sensible route to predicting $S(T)$ factors and thus to determining the scaling factor (proportional to the Einstein B -coefficient) from the best-fit straight line between n and S over the complete range of T . All of the C_2H_2 transitions of interest involve $\Delta v_4=\Delta v_5=1$ changes in vibrational quantum number. We therefore assume that all have the same (or similar) Einstein B -coefficients. The right hand axis in Fig. 14 thus provides estimates of the $S(T)$ factors for the transitions of interest involving levels with $v>0$. We estimate that the cumulative error in this procedure is $\sim 5\%$, which is well within the error associated with LIA measurements involving these weak lines.

- ¹D. G. Goodwin and J. E. Butler, in *Handbook of Industrial Diamonds and Diamond Films*, edited by M. A. Prelas, G. Popovici, and L. K. Bigelow (Dekker, New York, 1998), pp. 527–581 and references therein.
- ²J. Isberg, J. Hammersberg, E. Johansson, T. Wikstrom, D. J. Twitchen, A. J. Whitehead, S. E. Coe, and G. A. Scarsbrook, *Science* **297**, 1670 (2002).
- ³C. S. Yan, Y. K. Vohra, H. K. Mao, and R. J. Hemley, *Phys. Status Solidi A* **201**, R25 (2004).
- ⁴G. Bogdan, K. de Corte, W. Deferme, K. Haenen, and M. Nesládek, *Phys. Status Solidi A* **203**, 3063 (2006).
- ⁵Yu. A. Mankelevich, M. N. R. Ashfold, and J. Ma, *J. Appl. Phys.* **104**, 113304 (2008).
- ⁶M. N. R. Ashfold, P. W. May, J. R. Petherbridge, K. N. Rosser, J. A. Smith, Y. A. Mankelevich, and N. V. Suetin, *Phys. Chem. Chem. Phys.* **3**, 3471 (2001) and references therein.
- ⁷P. K. Bachmann, D. Leers, and H. Lydtin, *Diamond Relat. Mater.* **1**, 1 (1991) and references therein.
- ⁸T. Mitomo, E. Kondoh, and H. Ohtsuka, *J. Appl. Phys.* **70**, 4532 (1991).
- ⁹W. L. Hsu, M. C. McMaster, M. E. Coltrin, and D. S. Dandy, *Jpn. J. Appl. Phys., Part 1* **33**, 2231 (1994).
- ¹⁰M. C. McMaster, W. L. Hsu, M. E. Coltrin, D. S. Dandy, and C. Fox, *Diamond Relat. Mater.* **4**, 1000 (1995).
- ¹¹F. G. Celii, P. E. Pehrsson, H.-t. Wang, and J. E. Butler, *Appl. Phys. Lett.* **52**, 2043 (1988).
- ¹²F. G. Celii and J. E. Butler, *Annu. Rev. Phys. Chem.* **42**, 643 (1991).
- ¹³G. Lombardi, G. D. Stancu, F. Hempel, A. Gicquel, and J. Röpcke, *Plasma Sources Sci. Technol.* **13**, 27 (2004).
- ¹⁴G. Lombardi, K. Hassouni, G. D. Stancu, L. Mechold, J. Röpcke, and A. Gicquel, *Plasma Sources Sci. Technol.* **14**, 440 (2005).
- ¹⁵G. Lombardi, K. Hassouni, G. D. Stancu, L. Mechold, J. Röpcke, and A. Gicquel, *J. Appl. Phys.* **98**, 053303 (2005).
- ¹⁶A. Cheesman, J. A. Smith, M. N. R. Ashfold, N. Langford, S. Wright, and G. Duxbury, *J. Phys. Chem. A* **110**, 2821 (2006).
- ¹⁷R. F. Kazarinov and R. A. Suris, *Sov. Phys. Semicond.* **5**, 707 (1971).
- ¹⁸J. Faist, F. Capasso, D. L. Sivco, C. Sirtori, A. L. Hutchinson, and A. Y. Cho, *Science* **264**, 553 (1994).
- ¹⁹G. Duxbury, N. Langford, M. T. McCulloch, and S. Wright, *Chem. Soc. Rev.* **34**, 921 (2005).
- ²⁰J. Ma, J. C. Richley, M. N. R. Ashfold, and Yu. A. Mankelevich, *J. Appl. Phys.* **104**, 103305 (2008).
- ²¹L. S. Rothman, A. Barbe, D. C. Benner, L. R. Brown, C. Camy-Peyret, M. R. Carleer, K. Chance, C. Clerbaux, V. Dana, V. M. Devi, J.-M. Flaud, R. R. Gamache, A. Goldman, D. Jacquemart, K. W. Jucks, W. J. Lafferty, J.-Y. Mandin, S. T. Massie, V. Nemtchinov, D. A. Newnham, A. Perrin, C. P. Rinsland, J. Schroeder, K. M. Smith, M. A. H. Smith, K. Tang, R. A. Toth, J. Vander Auwera, P. Varanasi, and K. Yoshino, *J. Quant. Spectrosc. Radiat. Transf.* **82**, 5 (2003).
- ²²Y. Kabbadj, M. Herman, G. Di Lonardo, L. Fusina, and J. W. C. Johns, *J. Mol. Spectrosc.* **150**, 535 (1991).
- ²³J. Ma, M. N. R. Ashfold, and Yu. A. Mankelevich, *J. Appl. Phys.* **105**, 043302 (2009).
- ²⁴O. J. L. Fox, J. Ma, P. W. May, M. N. R. Ashfold, and Yu. A. Mankelevich, *Diamond Relat. Mater.* **18**, 750 (2009).
- ²⁵M. Herman, T. R. Huet, Y. Kabbadj, and J. Vander Auwera, *Mol. Phys.* **72**, 75 (1991).
- ²⁶G. Herzberg, *Molecular Spectra and Molecular Structure II. Infrared and Raman Spectra of Polyatomic Molecules* (Van Nostrand Reinhold, New York, 1945).